

Structural and Electrical Properties of Mechanothermally Synthesized NiFe_2O_4 Nanoceramics

C. BEHERA,^{1,2} PIYUSH R. DAS,¹ and R.N.P. CHOUDHARY¹

1.—Multifunctional Materials Research Laboratory, Department of Physics, Siksha “O” Anusandhan University, Bhubaneswar 751030, India. 2.—e-mail: cdbehera1986@gmail.com

NiFe_2O_4 nanoceramics were prepared by high-energy ball milling followed by a solid-state reaction technique. X-ray powder diffractometry, scanning electron microscopy, and impedance spectroscopy techniques were used to study preliminary structural, microstructural, and detailed electrical characteristics, respectively, of the nickel ferrite nanoceramics. The crystallite size of the fine (nanosize) powder of the compound was found to decrease after 30 h, 60 h, and 90 h of milling. It was also found that, at low temperatures and high frequencies, the relative permittivity and tangent loss of the material were size and milling time dependent. Detailed analysis of impedance spectroscopy data clearly showed the size dependence of the impedance characteristics and dielectric relaxation of the material. The temperature–frequency dependence of the alternating-current (ac) conductivity obeyed Jonscher’s universal power law.

Key words: Nanoceramics, XRD, spinel ferrite, impedance spectroscopy

INTRODUCTION

Although a large number of ferrites from different structural families (i.e., perovskites, spinels, hexaferrites, rare-earth/yttrium iron garnets, etc.) are now available, nickel ferrite (NiFe_2O_4) has a special position in the spinel structural family. The ferrimagnetism in this material originates from the magnetic moment of antiparallel spins between Fe^{3+} ions at tetrahedral sites and Ni^{2+} ions at octahedral sites. This ferrite has many industrial applications, including biomedical.¹ Although this material has a small magnetic coercivity value, it is chemically stable and mechanically hard, with good electrochemical performance.² Recently, NiFe_2O_4 (NFO) was identified as a material for use in negative electrodes for Li-ion batteries³ and supercapacitors.⁴ It is now a well-established fact that the particle/grain size and shape play an important role in tailoring the electrical, magnetic, and electrochemical properties of materials for device applications.^{5,6} Therefore, selection of suitable synthesis/fabrication and characterization

methods is highly desirable to obtain microsize and nanosize structures and particles.⁷ Besides this, nickel ferrite, as a semiconductor, has attracted much attention from researchers for the development of nanopowder and the structure of the material for technological applications. The aforementioned properties are dependent not only on the particle size but also on various other factors such as the chemical composition, preparation technique, stoichiometry, sintering time, temperature, and atmosphere, substitution of different ions, etc.⁸ Because of strong dipole–dipole interaction, there are some problems and challenges associated with utilization of nanocrystalline magnetic materials for devices. One of these is aggregation of nanoparticles due to their high surface reactivity.⁹ Moreover, nanofabrication lowers the coordination between atoms on surfaces, causing a reduction in the magnetic moment compared with bulk structures.¹⁰ Primary ferrite nanoparticles rapidly aggregate to form spherical clusters in order to minimize their surface energy. As a result, the fabrication and resulting properties of secondary architectures are strongly dependent on the morphological and structural features of the material. In the present work, an attempt was made

(Received December 24, 2013; accepted April 23, 2014; published online June 7, 2014)

to prepare NFO by a mechanical alloying technique (with different milling times) followed by thermal treatment, and to study the resulting structural and electrical (capacitive and resistive) properties in different experimental conditions.

EXPERIMENTAL PROCEDURES

Polycrystalline nickel ferrite (NFO) was prepared using high-purity, analytical reagent (AR)-grade nickel oxide (NiO; M/S HiMedia) and iron oxide (Fe₂O₃; M/S-Loba Chemie, India) at the required stoichiometry. These ingredients were mixed thoroughly in an agate mortar and pestle in dry (air) as well as wet (methanol) media. The mixed powder was ball-milled in a zirconium grinding jar of 250 ml capacity using 10-mm zirconium balls for different milling times (30 h, 60 h, and 90 h) in a planetary ball mill (PM 100; Retsch, Germany) at ball-to-mass ratio of 10:1 and 450 rpm in toluene medium. After each 30 h of milling, a small amount of the mixed powder was calcined at a relatively low temperature (800°C) compared with the mixed oxide method.¹¹ The preliminary crystal structure system, grain size, and crystallite size of the ball-milled powder samples were determined using the x-ray diffraction pattern (Miniflex; Rigaku, Japan) recorded with Cu K_α radiation ($\lambda = 1.5418$ Å) over a wide range of Bragg angle at room temperature. The calcined powders were mixed thoroughly with polyvinyl alcohol (PVA, binder) solution, then pressed into disk-shaped pellets (10 mm diameter, 1 mm to 2 mm thickness) at pressure of 5×10^6 kg/m². The pellets were sintered at 820°C for 4 h in air. The grain size and its distribution on the surface of the pellet samples were obtained by scanning electron microscopy (SEM, JSM model 6510; JEOL, USA). Highly conducting silver paint was used to form electrodes on both surfaces of the sintered ceramics for electrical measurements. The capacitance, dissipation factor, impedance, and related parameters were obtained as a function of temperature (30°C to 525°C) over a wide range of frequency (1 kHz to 1 MHz) using a computer-controlled phase-sensitive meter (PSM LCR, model 1735; N4L, UK) with a laboratory-designed/fabricated sample holder.

STRUCTURAL AND MICROSTRUCTURAL ANALYSES

Figure 1 shows the room-temperature XRD patterns of NFO powder samples milled for different durations. The diffraction patterns consist of a number of characteristic peaks. The broad reflection peaks indicate that the samples were composed of small particles. With increasing milling time, the width of the reflection peaks increased but the intensity decreased continuously, confirming that the crystallite or particle size of the powders decreased with increasing milling time. The crystallite size (P) of the milled samples was calculated from the broadening

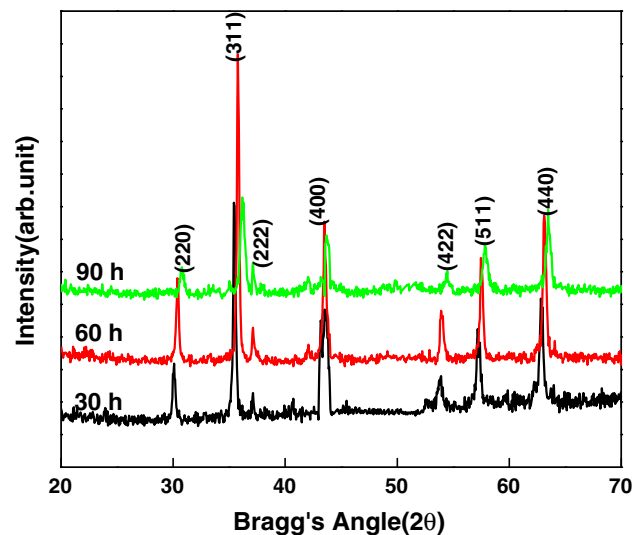


Fig. 1. XRD patterns of NiFe₂O₄ after different milling times.

of the reflection profile using the Debye–Scherrer formula: $P = \frac{0.89\lambda}{\beta \cos \theta}$, where β is the broadening (in radians) of a diffraction line measured at half-maximum intensity, $\lambda = 1.5406$ Å (the wavelength of Cu K_α radiation), and θ is the Bragg angle. The amount of broadening of the experimental XRD peaks suggested that a large number of defects were introduced into the samples with increasing milling time. Broadening of reflection lines can be caused not only by small particle or crystallite size but also by lattice strain, instrumental errors, dislocations, impurities, etc.¹² As powder samples were used to record the XRD patterns, broadening due to strain and other mechanical defects was ignored in the crystallite size calculation. The calculated crystallite size of the samples was 29 nm, 25 nm, and 21 nm for milling time of 30 h, 60 h, and 90 h, respectively. The reflections at 30.281°, 35.761°, 37.112°, 43.721°, 54.081°, 57.41°, and 63.241° (on the x -axis) were indexed to the (220), (311), (222), (400), (422), (511), and (440) planes of the face-centered cubic structure (with space group $Fd3m$), being highly consistent with reported data.¹³

The scanning electron micrographs in Fig. 2a–c show that, with increasing milling time, the grain size decreased continuously. The grain size of the samples was found to be in the range of 0.030 μ m to 0.061 μ m. In all samples, most of the grains were uniformly distributed on the surface of the pellet. The nature (size, distribution, and voids) of the grains clearly suggested that the pellet samples had high density (i.e., less voids).

DIELECTRIC STUDIES

Figure 3a–c shows the temperature dependence of the relative dielectric constant (ϵ_r) and loss tangent ($\tan \delta$) at various frequencies for the milled NFO samples. Both dielectric parameters (ϵ_r and

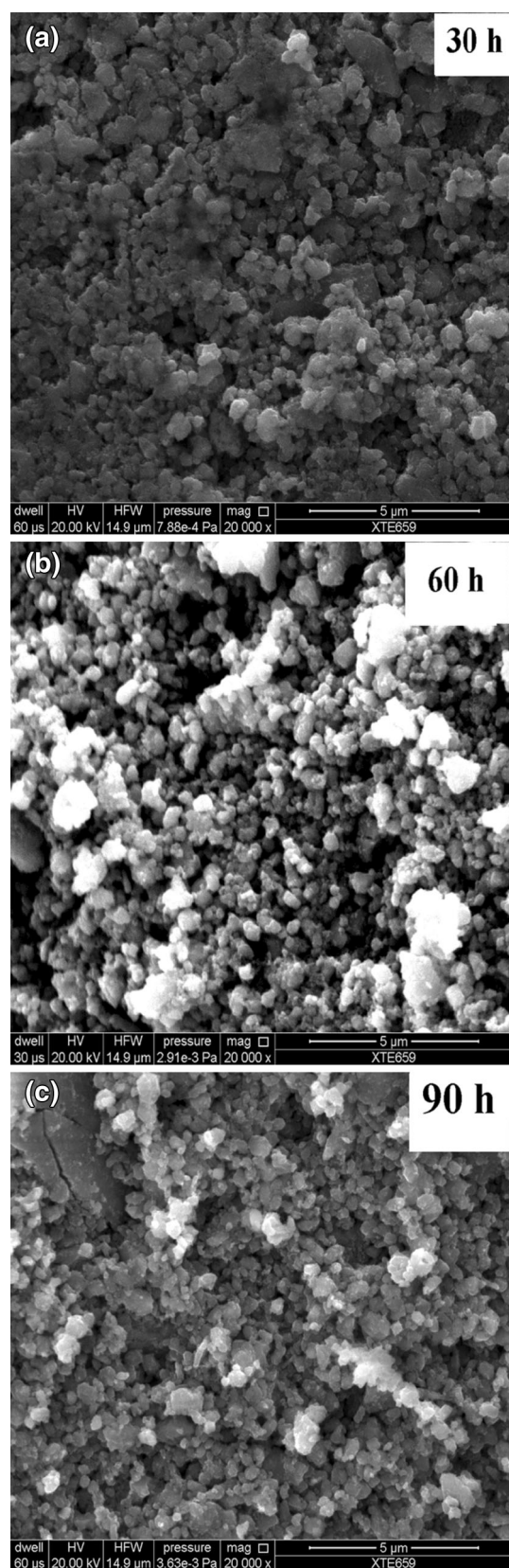


Fig. 2. SEM images of NiFe_2O_4 after milling time of (a) 30 h, (b) 60 h, and (c) 90 h.

$\tan \delta$) decrease with increasing frequency, which is a general feature of dielectric materials. It is a well-known fact that, at low frequency, all the different types of polarization (interfacial, dipole, atomic, ionic, electronic, etc.) exist in dielectrics. These types of polarization slowly vanish with increasing frequency, and as a result the dielectric constant decreases. There are some other reasons for the higher value of dielectric constant at low frequency. According to the Maxwell–Wagner interfacial polarization law,¹⁴ dispersion or a higher value of dielectric constant is observed at low frequency, which is in good agreement with Koop's phenomenological theory.¹⁵ This theory explains that the dispersion is a result of the inhomogeneous nature of the dielectric structure, being composed of two layers.¹⁵ The first layer is formed of large ferrite grains of highly conducting material, which is separated by the second, thin layer of relatively poorly conducting material (grain boundary). The grain boundaries are more effective at lower frequencies, while the grains are found to be more effective at higher frequencies. In ferrite materials, electrons being the majority charge carriers, the hopping mechanism of electrons takes place between Fe^{3+} ions and Fe^{2+} ions present at different crystallographic sites. The small value of ϵ_r at higher frequencies may be due to the fact that electron hopping between Fe^{3+} and Fe^{2+} ions at both octahedral and tetrahedral sites cannot follow the alternation of the ac electric field at these frequencies. Therefore, electrons have to pass through the well-conducting grains and poorly conducting grain boundaries. Since the grain boundaries offer high resistance, the electrons become crowded there, resulting in enhanced space-charge polarization. As a result, the material has a larger ϵ_r value in the low-frequency range. With increasing frequency, the direction of motion of the electrons changes rapidly. This hinders the movement of electrons inside the dielectric material, thereby reducing the charge accumulation at grain boundaries. Thus, lower space-charge polarization and relative permittivity are observed. Furthermore, ϵ_r gradually increases with increasing temperature, showing the same trend as observed for $\tan \delta$. The rate of increase of $\tan \delta$ in the material at low temperatures is slow, whereas at higher temperatures the increase is relatively sharper. This sharp increase in the value of $\tan \delta$ at higher temperatures is due to scattering of thermally activated charge carriers and the presence of some unknown defects (including oxygen vacancies) in the material. At higher temperatures, the domination of conductivity is responsible for the rise in $\tan \delta$ (Fig. 3a–c). With increasing milling time, the dielectric constant also continues to increase in the low-temperature/frequency region. The same trend is observed in the high-temperature/frequency region; For example,

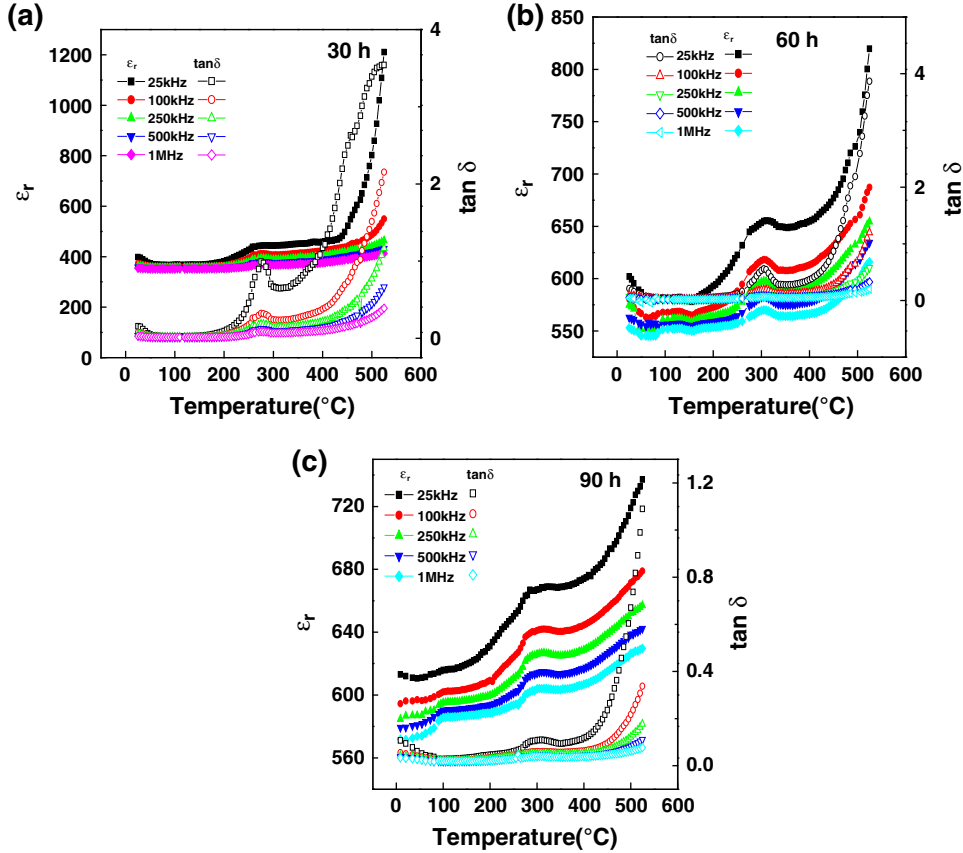


Fig. 3. Temperature dependence of ϵ_r and $\tan \delta$ at various frequencies for NiFe_2O_4 with milling time of (a) 30 h, (b) 60 h, and (c) 90 h.

the dielectric constant at 500°C is 402 (for 30 h), 598 (for 60 h), and 627 (for 90 h) at 1 MHz. As the composition, milling configuration, and annealing temperature were the same for all three samples with different milling times, the decrease in particle size is observed to be responsible for this enhancement of the dielectric constant. It is observed that, with increasing milling time, there is a remarkable change in the loss spectrum of the different samples. One observes an anomaly in both the relative dielectric constant (ϵ_r) and $\tan \delta$ at about 300°C, and the dielectric peak shifts towards lower temperature with increasing frequency.

IMPEDANCE SPECTRUM ANALYSIS

The impedance spectroscopy (IS) technique is based on analyzing the ac response of a system to a sinusoidal perturbation, with subsequent calculation of the impedance and related parameters as functions of the frequency of the perturbation at different temperatures. It is also a reliable technique to investigate the electrical properties and related conduction process of the material. The impedance properties of a material are highly related to its intragrain, intergrain, and electrode processes. The motion of the charge carriers affects the (i) dipolar orientation, (ii) space-charge formation,

and (iii) charge displacement. Thus, the complex impedance formalism allows one to separate out the contributions from the bulk, grain boundaries, and electrode effects/phenomena for the material at given temperature and frequency. Therefore, complex impedance spectroscopy (CIS) is a powerful nondestructive technique to investigate the electrical properties of a material over a wide range of frequency and temperature. The CIS technique correlates the electrical process with the microstructure of the material.^{16–19} Some impedance parameters of the material (i.e., capacitive and resistive components) lead to a succession of semicircles when represented on a Nyquist plot. Generally, the frequency dependence of the dielectric properties of a material can be described in terms of the following quantities:

$$\text{Complex dielectric constant : } \epsilon^* = \epsilon' - j\epsilon'', \quad (1)$$

$$\text{Complex impedance : } Z^* = Z' - jZ'' = R_s - \frac{j}{\omega C_s}, \quad (2)$$

$$\text{Dielectric modulus : } M^* = M' + jM'' = j\omega C_0 Z^*, \quad (3)$$

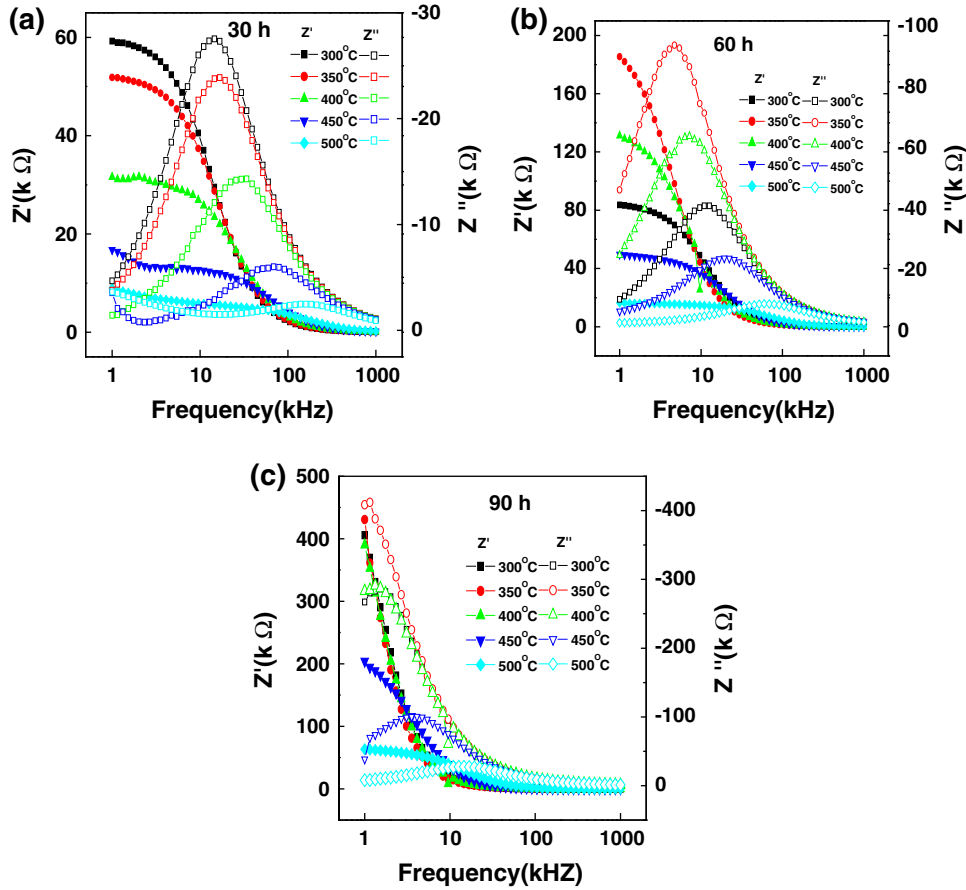


Fig. 4. Frequency and temperature dependence of Z' and Z'' for NiFe₂O₄ samples with milling time of (a) 30 h, (b) 60 h, and (c) 90 h.

$$\text{Dielectric loss : } \tan \delta = \frac{\varepsilon''}{\varepsilon'} = \frac{-Z'}{Z''} = \frac{M''}{M'}. \quad (4)$$

These parameters are related to each other. In these equations, ω is the angular frequency, ε_0 is the permittivity of free space, and R_s and C_s are the series resistance and capacitance, respectively. All the above expressions provide wide scope for graphical representation, since all of them can be used to calculate the complex impedance of the electrode–ceramic–electrode capacitor (demonstrated as the sum of a single RC circuit with parallel combination) as per the relation

$$Z^*(T) = Z_0(T) \int \frac{Y(\tau, T) d\tau}{1 + j\omega\tau}. \quad (5)$$

This complex equation can be resolved into two components (the real and imaginary part), expressed as

$$Z'(\omega, T) = Z_0(T) \int \frac{Y(\tau, T) d\tau}{1 + \omega^2\tau^2} \quad (6)$$

and

$$Z''(\omega, T) = Z_0(T) \int \frac{(\omega\tau)^* Y(\tau, T) d\tau}{1 + \omega^2\tau^2}, \quad (7)$$

where $\tau = R_b C_b$ represents the relaxation time, T is the time period, and $Y(\tau, T)$ is the distribution function of the relaxation time. The variation of the imaginary part of the complex impedance $Z''(\omega, T)$ provides information about the distribution function $Y(\tau, T)$.

Figure 4a–c shows the frequency variation of the real and imaginary parts of the impedance (Z' and Z'') for the NFO samples with different milling times at different temperatures. The value of Z' decreases with increase in frequency, whereas it increases with rise in temperature. The magnitude of Z' decreases with increasing temperature in the low-frequency range, and the data merge in the high-frequency region irrespective of temperature. This nature of the plot may be due to the release of space charge.¹⁷ The reduction in the barrier properties of the material with rise in temperature may be a factor responsible for the enhancement of the ac conductivity of the material at higher frequencies.^{20,21} Further, in the low-frequency region, there is a decrease in the magnitude of Z' with rise in temperature, showing negative temperature coefficient

of resistance (NTCR) behavior. This behavior changes drastically in the high-frequency region, showing complete merging of the Z' plots above a certain frequency. At high frequency, the values of Z' at different temperatures coincide, implying the possible release of space charge.¹⁹ A peak at a particular frequency (at which Z' becomes independent of frequency) was observed, shifting to higher frequency with increasing temperature. This shift in the Z' plateau indicates the existence of a frequency relaxation process in the material. The curves display a single relaxation process and indicate an increase in the ac conductivity with increase in temperature and frequency.²⁰ A monotonic decrease in Z'' in the low-temperature region with the appearance of peaks in the loss spectrum at high temperatures and a significant increase in peak broadening with increasing temperature are the special features of the loss spectrum. The absence of peaks in the loss spectrum in the low-temperature range (up to 275°C) for all the milled samples suggests the lack of current dissipation in this temperature region. The pattern shows peaks at a particular frequency, which is different for the samples with different milling times, describing the type and strength of the electrical relaxation phenomenon in the material.^{20–22} The value of Z'' reaches a maximum (Z''_{\max}) at 350°C. The Z''_{\max} value shifts to higher frequency with increasing temperature, indicating an increase of the tangent loss of the sample. The significant increase in the broadening of the peaks with increase in temperature suggests the existence of a temperature dependence of the electrical relaxation phenomenon in the material. The relaxation process may be due to the presence of electrons/immobile species at low temperatures and defects/vacancies at higher temperatures. The asymmetric broadening of the peaks suggests a spread of the relaxation time with two equilibrium positions. The peak heights are proportional to the bulk resistance (R_b) and can be explained using the equation $Z'' = R_b[\omega\tau/(1 + \omega^2\tau^2)]$ for plots of Z'' versus frequency. Furthermore, the magnitude of Z'' gradually decreases with a shift in the peak frequency towards higher frequency, finally merging in the high-frequency region. This is an indication of accumulation of space charge in the material.²³

It is observed that, with increasing milling time, both Z' and Z'' first increase with rise in temperature, then remain constant above 400°C. These parameters are also independent of frequency. The value of Z''_{\max} shifts to higher frequency with increasing milling time of the material, indicating a decrease of the tangent loss. A significant increase in the broadening of the peaks with increasing milling time suggests enhancement of the electrical relaxation phenomenon in the material.

Figure 5a–c shows complex impedance spectra (Nyquist plots) for the compound measured at different temperatures (>300°C) over a wide range

of frequency (100 Hz to 1 MHz). The impedance properties of the material are characterized by semicircular arcs whose pattern of evolution changes with temperature. The intercept of the semicircles with the real axis (x -axis) and their number in the spectrum provide information regarding the kind of electrical processes occurring within the material. The correlation between the arcs and the microstructure of the material can be established by considering an equivalent electrical circuit. The experimental and theoretically fit data were investigated using commercially available software (ZSimpWin version 2.0) for an ideal Debye-like response. The equivalent circuit (Fig. 5a–c) for the fitting curves consists of a parallel combination of CR and CQR , where Q is known as a constant-phase element (CPE). Using the fit curves, the values of the bulk resistance (R_b), grain-boundary resistance (R_{gb}), bulk capacitance (C_b), and grain-boundary capacitance (C_{gb}) at different temperatures were calculated, as compared in Table I. The semicircular arcs of the impedance pattern were mainly attributed to a parallel combination of resistance and capacitance. As the temperature increases from room temperature, the arc progressively becomes semicircular with a shift of the center towards the origin of the complex plane plot. With further increase in temperature, the slope of the line decreases, and it bends towards the Z' -axis (above 300°C), thus a semicircle could be traced indicating the increase in conductivity of these samples.²⁰ The presence of the semicircular arcs for temperatures above 300°C suggests that the electrical processes in the material are basically due to the contributions from the bulk material (grain interior) and grain boundaries. With increasing milling time, the radius of the semicircular arc generally increases. A comparative study of the Nyquist plots at 500°C is shown in Fig. 5d. The capacitive and resistive parameters at 300°C to 500°C for the samples milled for 30 h, 60 h, and 90 h are presented in Table I, providing some fundamental ideas on the disorder present in the nanoceramics.

For an ideal, Debye-type relaxation, a perfect semicircle with center on the Z' -axis is expected. In the studied material, depressed semicircles corresponding to non-Debye-type relaxation were observed. A distribution of relaxation times is expected in the material instead of a single relaxation time.^{20,21} The intercept of each semicircle with the real, Z' -axis gives the value of the bulk and grain-boundary contributions to the resistance/impedance. The semicircles in the impedance spectrum have a characteristic peak occurring at a unique relaxation frequency, usually referred to as the resonance frequency (f_r , or $\omega_r = 2\pi f_r$). It can be expressed as $\omega_r RC = \omega_r \tau = 1$ and thus $f_r = 1/2\pi RC$, where τ is the relaxation time. The relaxation time due to the bulk effect (τ_b) was calculated using the equation $\omega_r \tau_b = 1$, or $\tau_b = 1/2\pi f_r$.

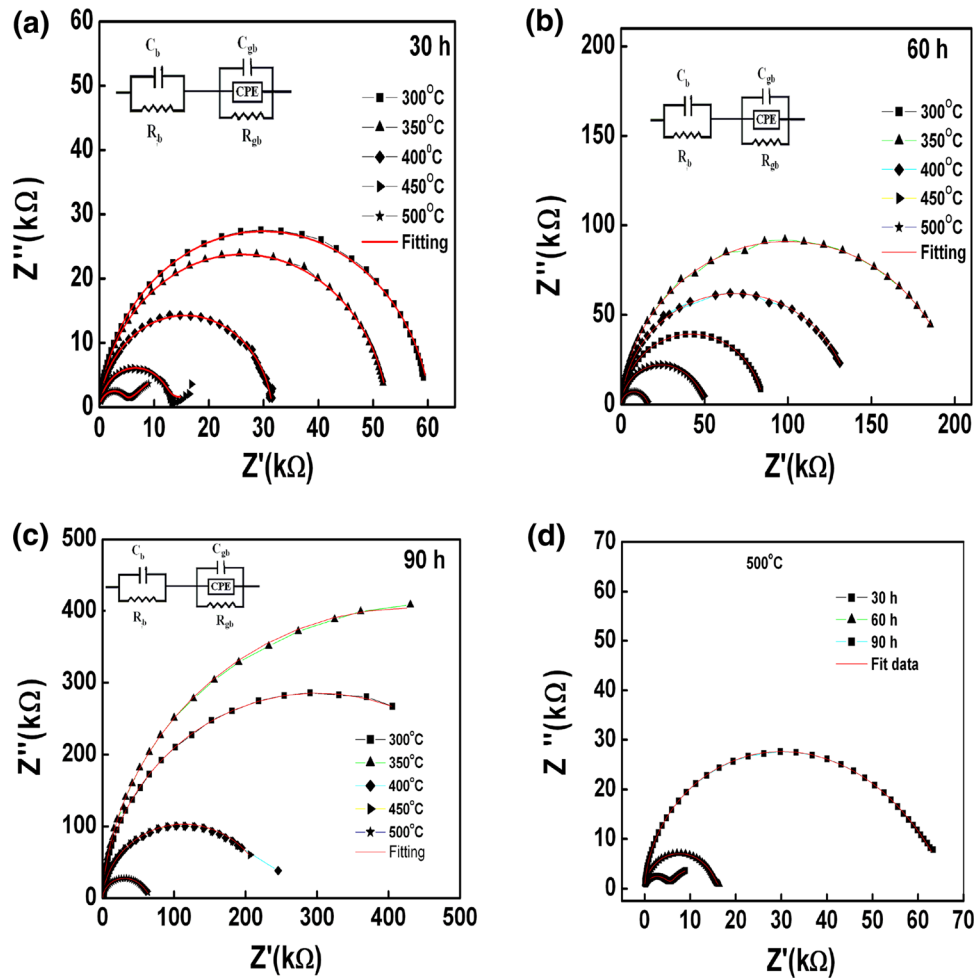


Fig. 5. Nyquist plot for (a) 30 h, (b) 60 h, and (c) 90 h milled NiFe_2O_4 samples at different temperatures and (d) their comparison at 500°C .

Table I. Comparison of impedance fitting parameters (R_b , C_b , R_{gb} , C_{gb}) at different temperatures for NiFe_2O_4 samples with different milling times

Milling Time (h)	Temperature ($^\circ\text{C}$)	C_b (nF)	R_b (Ω)	C_{gb} (nF)	R_{gb} (Ω)
30	300	1.012×10^{-10}	4.12×10^4	1.002×10^{-10}	4.324×10^4
	350	1.032×10^{-10}	3.54×10^6	1.047×10^{-10}	5.275×10^4
	400	1.056×10^{-10}	3.161×10^4	2.012×10^{-10}	3.867×10^4
	450	2.236×10^{-10}	1.047×10^4	3.964×10^{-10}	1.694×10^4
	500	1.127×10^{-7}	48.16	1.645×10^{-10}	7.499×10^4
60	300	1.616×10^{-7}	772.9	1.045×10^{-10}	8.853×10^4
	350	4.303×10^{-7}	1.043×10^{-5}	1.191×10^{-10}	2.024×10^5
	400	9.282×10^{-7}	1.265×10^{-6}	1.202×10^{-10}	1.389×10^5
	450	4.039×10^{-8}	8.079	2.829×10^{-10}	2.116×10^4
	500	6.634×10^{-8}	27.38	1.567×10^{-10}	1.849×10^4
90	300	1.666×10^{-8}	30.6	1.135×10^{-10}	6.03×10^5
	350	1.438×10^{-8}	2.173	1.221×10^{-10}	8.415×10^5
	400	2.187×10^{-7}	0.01	1.25×10^{-10}	6.269×10^5
	450	6.797×10^{-7}	18	1.43×10^{-10}	2.345×10^5
	500	2.228×10^{-7}	17.06	2.754×10^{-10}	3.83×10^4

COMPLEX ELECTRIC MODULUS ANALYSIS

Figure 6a–c shows the variation of M' and M'' with frequency at selected temperatures ($>300^\circ\text{C}$). The value of M' approaches zero with decreasing frequency with monotonic dispersion, whereas with

rise in frequency, the values of M' coincide, indicating negligibly small contributions from electrode polarization. The value of M' is maximum at a particular frequency called the relaxation frequency (R_f), and the M' maximum shifts to higher frequency

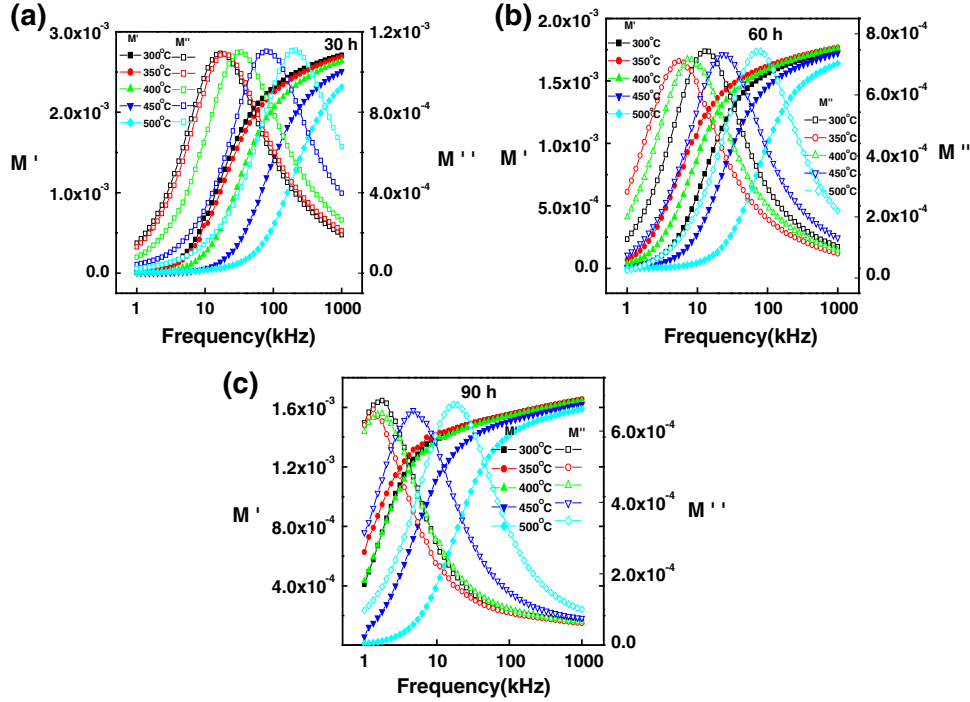
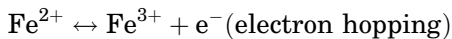
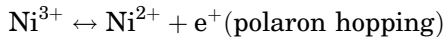


Fig. 6. Variation of M' and M'' with frequency for NiFe_2O_4 samples milled for (a) 30 h, (b) 60 h, and (c) 90 h.

as the temperature increases. The relaxation time can be calculated using the relation $2\pi R_f \tau_m = 1$, which is a condition for the transition from long-range to short-range mobility. This may be due to the presence of conduction phenomenon and short-range mobility of charge carriers. This implies that there is a lack of restoring force for flow of charges under the influence of a steady electric field.²³ The M''_{max} peak shifts to the higher frequency side. This nature of the dielectric relaxation suggests that the hopping mechanism of charge carriers dominates intrinsically at higher temperatures in a thermally activated process. Asymmetric broadening of the peak indicates a spread of relaxation with different time constants, which suggests the occurrence of non-Debye-type relaxation in the material.²⁴

AC CONDUCTIVITY STUDY

Electrons in nickel ferrite are localized, hence the electrical conductivity increases with increase in temperature due to hopping of charge carriers. Electrical conduction in NFO is due to electron hopping between Fe^{2+} and Fe^{3+} ions and hole hopping between Ni^{3+} and Ni^{2+} ions at B sites^{25,26}



The dielectric data were used to calculate the ac conductivity using the relation $\sigma_{\text{ac}} = \omega \epsilon \epsilon_0 \tan \delta$,

where ϵ_0 is the dielectric permittivity of free space and other parameters have their usual meanings. The activation energy E_a , based on a thermally activated process, can be calculated using the relation $\sigma_{\text{ac}} = \sigma_0 \exp(-E_a/kT)$, where k is the Boltzmann constant and σ_0 is a preexponential factor. The temperature dependence of the ac conductivity of different milled samples at different frequencies is shown in Fig. 7a–c. In the Arrhenius plot ($\log \sigma_{\text{ac}}$ versus $1000/T$) the value of $\log \sigma_{\text{ac}}$ increases linearly with increase in temperature. The estimated (using linear fitting) activation energy value in the high-temperature region (300°C to 500°C) at different frequencies is compared in Table II. For each frequency in the plots, the occurrence of different slopes in different temperature regions shows the presence of multiple conduction processes with different activation energies in the samples.^{27,28} The value of σ_{ac} decreases with increasing milling time. The conductivity decreases with milling time because of the decrease in grain size, and also due to the reduction in the number of Fe^{3+} – Fe^{2+} pairs at octahedral sites arising from the partial displacement of Fe^{3+} ions from octahedral to tetrahedral sites.²⁹ The activation energy due to electron hopping is on the order of 0.4 eV. The intermediate activation energy value (0.58 eV to 0.77 eV) is due to hopping of holes in addition to electron hopping. The anion vacancies are expected to give the higher activation energy (~ 1.03 eV). This activation energy value is characteristic of diffusion of oxygen vacancies.²⁹

To get a better understanding of the conduction mechanism in the material, Jonscher's universal

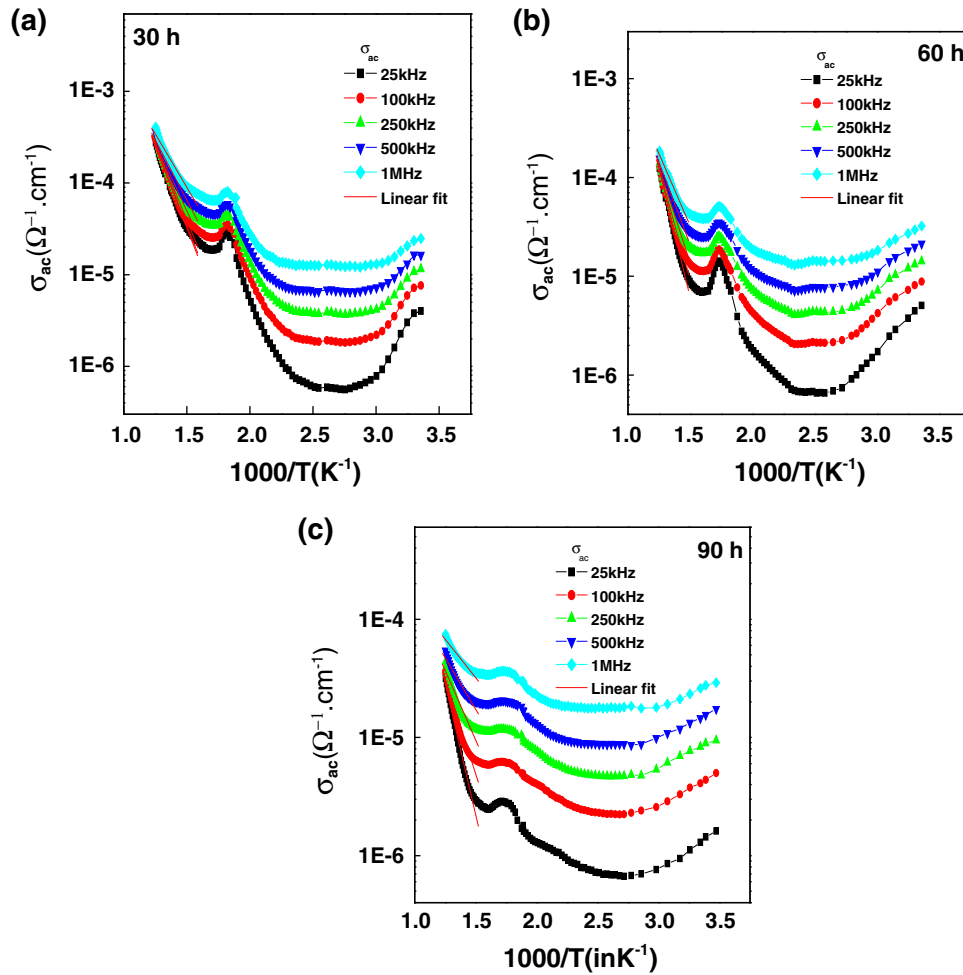


Fig. 7. Variation of σ_{ac} with inverse absolute temperature for NiFe₂O₄ samples milled for (a) 30 h, (b) 60 h, and (c) 90 h.

Table II. Activation energy of NiFe₂O₄ with different milling times at different frequencies

Milling Time (h)	Frequency (Hz)	Activation Energy (eV)
30	25 k	0.7029
	100 k	0.6954
	250 k	0.6650
	500 k	0.5896
	1 M	0.4626
60	25 k	1.0353
	100 k	0.9053
	250 k	0.7763
	500 k	0.6651
	1 M	0.6535
90	25 k	0.8803
	100 k	0.6349
	250 k	0.4677
	500 k	0.3455
	1 M	0.2585

power law^{30,31} was used. The total conductivity of the material can be obtained as $\sigma_T(\omega) = \sigma(0) + \sigma_1(\omega) = \sigma(0) + A\omega^n$, where $\sigma(0)$ is the frequency-independent

term giving the direct-current (dc) conductivity and $\sigma_1(\omega)$ is the purely dispersive component of the ac conductivity, having a characteristic power-law behavior in terms of frequency (ω). The value of the exponent lies between zero and one. The parameter n is frequency independent but temperature and material dependent. The preexponential factor A determines the polarizability strength and is temperature dependent.

Figure 8a–c shows the variation of σ_{ac} with frequency at selected high temperatures with nonlinear model fitting using Jonscher's power law. The value of σ is frequency dependent in the high-frequency region and independent in the low-frequency region. Extrapolation of the low-frequency σ_{ac} gives σ_{dc} . However, the increasing trend of σ_{ac} with rise in frequency (in the low-frequency region) may be due to disordering of cations between neighboring sites and the presence of space charge. In the high-frequency region, the curves approach each other. The curves exhibit a low-frequency dispersion phenomenon, obeying Jonscher's power-law equation. The origin of the frequency dependence of the conductivity lies in the

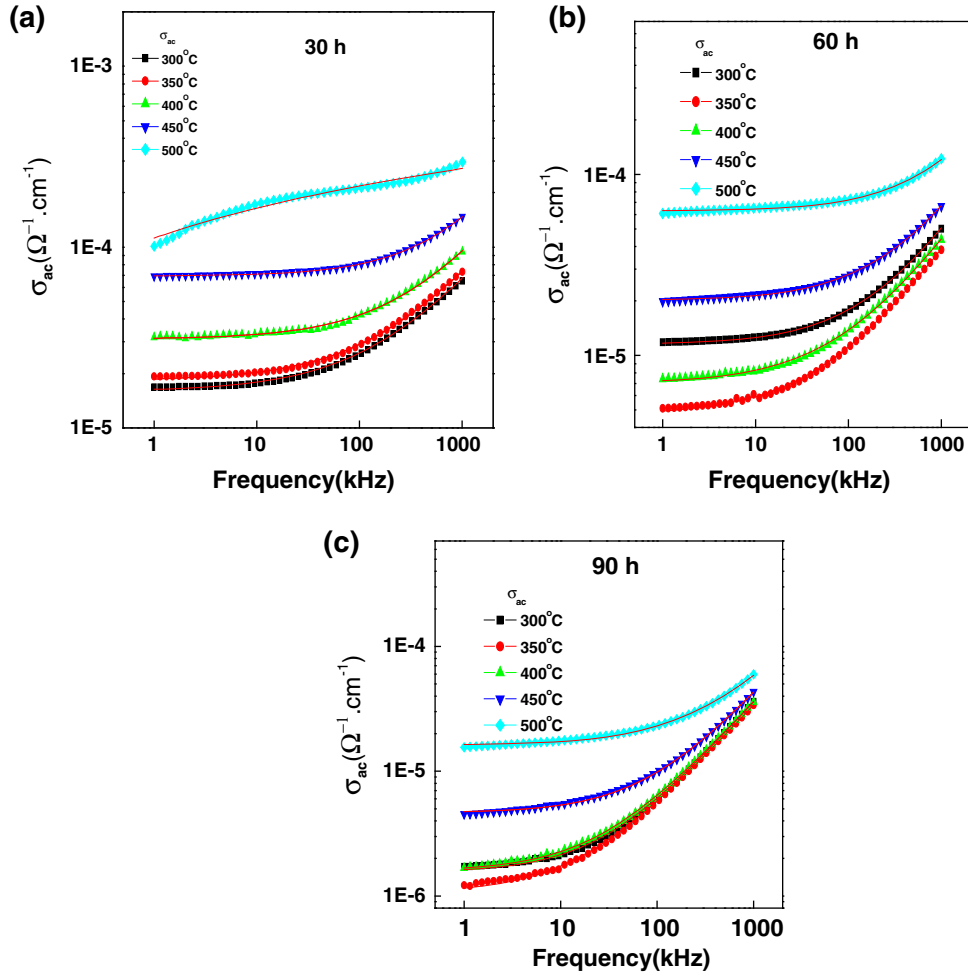


Fig. 8. Frequency dependence of ac conductivity of NiFe_2O_4 with milling time of (a) 30 h, (b) 60 h, and (c) 90 h.

relaxation phenomena arising due to mobile charge carriers.³¹ When a mobile charge carrier hops to a new site from its original position, it remains in a state of displacement between two potential-well energy minima. Also, the conduction behavior of the material obeys the power law $\sigma(\omega) \propto \omega^n$, with a slope change governed by n in the low-temperature region. A small value of n (< 1) suggests the involvement of translational motion with sudden hopping, whereas a larger value of n (> 1) suggests the involvement of localized hopping without the species leaving the neighborhood. The frequency at which the change in slope takes place is known as the hopping frequency of polarons (up), and is temperature dependent. From nonlinear fitting it is found that the motion of charge carriers is translational because of the small value of n (< 1).^{32,33} The nonlinear fitting data for different milling times and at different temperatures are presented in Table III. The dc conductivity increases with rise in temperature, as expected.

Table III. Comparison of frequency/temperature-dependent A and n values of NiFe_2O_4 with different milling times

Milling Time (h)	Temperature (°C)	A	n
30	300	2.8287×10^{-9}	0.710
	350	2.7081×10^{-9}	0.718
	400	1.7681×10^{-9}	0.760
	450	1.7614×10^{-9}	0.760
	500	1.7246×10^{-9}	0.770
60	300	7.295×10^{-10}	0.788
	350	1.5639×10^{-9}	0.723
	400	1.463×10^{-9}	0.733
	450	9.6153×10^{-10}	0.781
	500	1.0203×10^{-9}	0.792
90	300	1.7088×10^{-10}	0.884
	350	2.911×10^{-10}	0.841
	400	2.713×10^{-10}	0.868
	450	7.1427×10^{-10}	0.795
	500	1.7246×10^{-9}	0.770

CONCLUSIONS

NiFe₂O₄ nanoceramic samples were synthesized by high-energy ball milling followed by low-temperature heating. Formation of face-centered cubic (FCC) NiFe₂O₄ phase with inverse spinel structure was confirmed by preliminary structural analysis. The crystallite size of the material was calculated using Scherrer's equation. With increasing milling time, the crystallite size of the sample decreased. SEM showed a uniform distribution of grains on the surface of pellet samples. The grain size was found to be in the range of 0.030 μm to 0.061 μm . The ac conductivity increased with increase in temperature but decreased with increase in milling time. The impedance studies showed the presence of grains (bulk) and grain boundaries in all the ceramic samples milled for 30 h, 60 h, and 90 h. The existence of NTCR in the material was observed. Modulus analysis indicated that the material exhibits non-exponential-type conductivity relaxation. Experimental impedance data were used to estimate the electrical conductivity of the material. An equivalent circuit was used to demonstrate the electrical phenomena occurring inside the material. The ac conductivity obeys Jonscher's universal power law. The impedance spectroscopy of the material confirms the origin of the relaxation mechanism in the system.

ACKNOWLEDGEMENT

The authors gratefully acknowledge the grant received from DRDO (No. ERIP/ER/1102202/M/01/1438, dated 25/07/2012), Government of India to carry out this work.

REFERENCES

1. S. Maensiri, C. Masingboon, B. Banjong, and S. Seraphin, *Scr. Mater.* 56, 797 (2007).
2. B. Viswanathan and V.R.K. Murthy, *Ferrite Materials: Science and Technology* (New Delhi: Narosa, 1990).
3. H. Zhao, Z. Zheng, K. Wai, and S. Wang, *Electrochem. Commun.* 9, 2606 (2007).
4. P. Sen and A. De, *Electrochem. Acta* 55, 4677 (2010).
5. Y. NuLi, P. Zhang, Z. Guo, and H. Liu, *Electrochem. Soc.* 155, 196 (2008).
6. H.J. Ahn, H.C. Choi, K.W. Park, S.B. Kim, and Y.E. Sung, *J. Phys. Chem. B* 108, 9815 (2004).
7. Y. Mao, T.J. Park, F. Zhang, H. Zhou, and S.S. Wong, *Small* 3, 1122 (2007).
8. J.L. Berchmans, R.K. Selvan, and C.O. Augustin, *Mater. Lett.* 58, 1928 (2004).
9. H. Srikanth, R. Hajndl, C. Chirinos, J. Sanders, A. Sampath, and T. Sudarshan, *Appl. Phys. Lett.* 79, 3503 (2001).
10. R. Kodama, *Magn. Nanoparticles* 200, 359 (1999).
11. J. Du, G. Yao, Y. Liu, J. Ma, and G. Zu, *Ceram. Int.* 38, 1707 (2012).
12. G.P. Lopez and S.P. Silveti, *Phys. B* 354, 144 (2004).
13. M.R. Phadatare, A.B. Salunkhe, V.M. Khot, C.I. Sathish, D.S. Dhawale, S.H. Pawar, *J. Alloys Compd.* 546, 314 (2013).
14. R.C. Kambale, Y.A. Park, N. Hur, K.Y. Rajpure, and S.S. Suryavanshi, *J. Korean Phys. Soc.* 59, 3385 (2011).
15. C.G. Koops, *Phys. Rev.* 83, 121 (1951).
16. S. Sen and R.N.P. Choudhary, *Mater. Chem. Phys.* 87, 256 (2004).
17. S. Brahma, R.N.P. Choudhary, and A.K. Thakur, *Phys. B* 355, 188 (2005).
18. J.R. Macdonald, *Impedance Spectroscopy Emphasizing Solid Materials and Systems (Chapter 4)* (New York: Wiley, 1987).
19. J. Suchanicz, *Mater. Sci. Eng. B* 55, 114 (1998).
20. V. Provenzano, L.P. Boesch, V. Volterra, C.T. Moynihan, and P.B. Macedo, *J. Am. Ceram. Soc.* 55, 492 (1972).
21. H. Jain and C.H. Hsieh, *J. Non-Cryst. Solids* 172, 1408 (1994).
22. S. Pattanayak, B.N. Parida, P.R. Das, and R.N.P. Choudhary, *Appl. Phys. A* 112, 387 (2013).
23. S. Sen, R.N.P. Choudhary, and P. Pramanik, *Phys. B* 387, 56 (2007).
24. B. Behera, P. Nayak, and R.N.P. Choudhary, *J. Alloys Compd.* 436, 226 (2007).
25. I.M. Hodge, M.D. Ingram, and A.R. West, *J. Electroanal. Chem.* 58, 429 (1975).
26. A.M. Abdeen, *J. Magn. Magn. Mater.* 192, 121 (1999).
27. B. Senthilkumar, R.K. Selvan, P. Vinobabu, I. Perelshtein, and A. Gedanken, *Mater. Chem. Phys.* 130, 285 (2011).
28. R.N.P. Choudhary, D.K. Pradhan, C.M. Tirado, G.E. Bonilla, and R.S. Katiyar, *J. Mater. Sci.* 42, 7423 (2007).
29. N. Sivakumar, A. Narayanasamy, N. Ponpandian, J.M. Greneche, K. Shinoda, B. Jeyadevan, and K. Tohji, *J. Phys. D* 39, 4688 (2006).
30. C. Behera, R.N.P. Choudhary, and P.R. Das, *J. Mater. Sci.* 25, 2086 (2014).
31. A.K. Jonscher, *Nature* 267, 673 (1977).
32. C.K. Suman, K. Prasad, and R.N.P. Choudhary, *J. Mater. Sci.* 41, 369 (2006).
33. K. Funke, *Solid State Chem.* 22, 111 (1993).